Transfer Learning Framework for Impedance Characterization of Modular Multilevel Converters

Rane, Rahul; Kermansaravi, Azadeh; Vergara, Pedro P.; Lekić, Aleksandra

DOI
10.1109/TIA.2025.3529826

Publication date
2025

Document Version
Final published version

Published in
IEEE Transactions on Industry Applications

Transfer Learning Framework for Impedance Characterization of Modular Multilevel Converters

Rahul Rane, Azadeh Kermansaravi, Pedro P. Vergara, *Senior Member, IEEE*, and Aleksandra Lekić, *Senior Member, IEEE*

***Abstract*—The widespread use of modular multilevel converters (MMCs) in the evolution of complex power grids presents new challenges for grid stability. MMCs have highly nonlinear impedance characteristics due to their complex internal dynamics and intricate control architectures. Due to practical constraints, physics-based models cannot accurately compute these impedances, and the use of closed-box measurement techniques is time-consuming, resulting in a limited amount of data available for impedance characterization. Thus, using current methods to estimate impedances over a wide range of operating points can be unreliable. This paper presents a transfer learning-based framework for MMC impedance characterization using system-level parameters as operating point variables. The proposed approach predicts both AC and DC side impedances simultaneously by extrapolating impedances derived using state-space modeling approaches to real-time electromagnetic transient (EMT) simulations. Finally, the method is evaluated on a practical converter from the CIGRE B4 DC grid test system for various types of controllers and scenarios involving unknown parameters.**

***Index Terms*—HVDC, impedance model, machine learning, MMC, real-time simulation.**

I. Introduction

POWER electronic-based voltage source converters, notably modular multilevel converters (MMCs), have become increasingly significant in the power grid. This trend is driven by the growing interest in developing interconnected systems and the rise of renewable energy resources [1]. As the proportion of voltage source converters in the power grid increases, ensuring the stability and desired performance of the power system across a wide range of operating points is critical. However, the interaction between the converter's internal dynamics, control loops, and the rest of the grid can lead to stability issues on both the AC and DC sides [2], [3].

Impedance-based stability analysis is a prominent method for effectively identifying the interactions between the converter and the rest of the grid. The changing operating conditions of the converter result in varying impedance responses, requiring accurate modeling to conduct stability analysis [4], [5]. Moreover, the impedance characteristics of converters vary significantly depending on the controllers in use, such as phase-locked loop (PLL), active and reactive power control, and DC voltage control. Accurately estimating impedance characteristics under uncertain scenarios by considering multiple operating points and control types is crucial for analyzing system stability at the point of common coupling (PCC) using the generalized Nyquist stability criterion (GNC) [6].

Small-signal models derived from physics, mathematical formulations, and circuit analysis can determine the impedance characteristics of voltage source converters across various operating points, assuming all physical parameters are known. However, most existing studies have primarily focused on either the AC or the DC system, often neglecting the influence of the entire system [4], [5], [7], [8]. Studies in [9], [10], [11] show that both the AC and DC sides have similar properties in the presence of high-frequency interactions, therefore it is important to include both sides in the analysis. Nonetheless, developing such small-signal models requires a deep understanding of various system aspects, including control structure parameters and measurement filters. These models often overlook several nonlinearities such as control dead-time, sampling error, digital delay, variable frequency switching, and a nonlinear control framework [12]. Additionally, the practical implementation of hardware and software introduces deviations and non-idealities in physical parameters, significantly impacting converter impedances [12], [13]. Consequently, the reliability and accuracy of small-signal models are limited, especially for converters with complex control structures.

The closed-box impedance measurement techniques can effectively determine converter impedances without system parameters or control structures knowledge [2], [14], [15]. However, conducting impedance measurements or simulations across various operating points demands substantial human labor and computational resources since they typically rely on signal processing methods and electromagnetic transient (EMT) simulations [12]. Furthermore, obtaining both AC and DC side impedances can significantly increase the time and resources required. Therefore, a computationally efficient and precise method is needed to acquire converter impedances for both AC and DC sides.

Received 6 June 2024; revised 8 September 2024; accepted 16 October 2024. Date of publication 14 January 2025; date of current version 4 April 2025. Paper 2024-CDPA-0538.R1, approved for publication in the IEEE Transactions on Industry Applications by the Convergence of Data-driven and Physics-based Approaches in Power System Analysis, Optimization, and Control of the IEEE Industry Applications Society. This work was supported by NWO Veni Project SAFE-GRID through Project Number 20248. *(Corresponding author: Rahul Rane.)*

The authors are with the Intelligent Electrical Power Grids (IEPF) Section, Electrical Sustainable Energy, Delft University of Technology, 2628 CD Delft, The Netherlands (e-mail: rahulmrane@yahoo.com).

Color versions of one or more figures in this article are available at https://doi.org/10.1109/TIA.2025.3529826.

Digital Object Identifier 10.1109/TIA.2025.3529826

In recent years, there has been a growing interest in applying machine learning techniques to power grid analysis. [16] proposes a method utilizing artificial neural networks (ANNs) to predict impedance characteristics accurately across various operating conditions. However, this approach relies heavily on extensive impedance measurements, making it data-intensive. To mitigate this dependency, [17] proposes a physics-informed neural network model that leverages the inherent physical properties of two-level voltage source converters, significantly reducing the training effort needed. These methods, however, focus solely on impedance variations along a single operating point variable. In contrast, [18] and [12] extend the analysis to include a broader range of operating point variables, such as AC side voltage, active power, and reactive power at the AC side terminal. In addition, these works present a transfer learning-based methodology using a small-signal model to estimate the impedances of a two-level converter. Notably, none of these prior studies address the DC side impedances.

As the deployment of MMC-based high voltage direct current (HVDC) systems escalates, thorough analysis and precise estimation of their impedance characteristics become essential. MMCs have distinct internal dynamics compared to conventional two-level converters, introducing harmonic distortions into the system. These distortions significantly influence impedance characteristics due to their nonlinear relationship with the operating point. To the best of the authors' knowledge, there are limited studies on applying data-driven approaches for estimating impedances in MMC-based converters. The work in [19] presents a transfer learning-based approach with ANNs to characterize the AC side impedances of an MMC, comprising only of the inner control loops. Similar to [16] and [17], the operating point is defined by a single variable. In [20], an ANN-based method is used to predict the impedances for stability assessment of wind farms integrated with MMCs. However, their methodology is data-intensive and does not include all control loops. Practical high-power MMC systems typically feature complex control structures comprising outer and inner control loops and measurement filters. Consequently, the impedances vary considerably, rendering previous methods unsuitable. Moreover, estimating impedances across a broad spectrum of operating points, such as AC side voltage, active power, reactive power at the AC terminal, and DC side voltage, is crucial for MMC-based systems.

This paper overcomes the limitations of the previous methodologies by providing a more comprehensive approach and building on top of the transfer learning approach introduced in [12] and [19]. The proposed approach assesses both the AC and DC side impedances of MMCs controlled using power and DC voltage control based on the operating points, which include the AC side voltage V_{ac}, active power P_{ac}, reactive power Q_{ac}, and DC side voltage V_{dc} at the respective terminal. The primary concept of this study involves pre-training the ANN model with a diverse dataset of operating samples derived from a linear time-invariant (LTI) small-signal model. Subsequently, a smaller dataset obtained from real-time EMT simulations conducted using real time digital simulator (RTDS®) simulators is utilized to fine-tune the ANN model and enhance its accuracy significantly. Leveraging the LTI model assists in fulfilling the substantial data requirements of ANNs. Moreover, rather than training a single ANN model throughout the entire frequency range of 1 to 1000Hz, three smaller ANN models are used, each tuned to the impedance characteristics determined by the operating points and frequency in a specific range. A practical MMC converter sourced from the CIGRE B4 DC grid test system [21] serves as the testbed for developing the impedance-based model. This approach enables accurate impedance identification with smaller ANN architectures and a reduced amount of simulated data.

The main contributions of this paper are listed below:

- A transfer learning framework is introduced, which combines LTI state-space modeling and closed-box impedance measurements for accurate impedance estimation of MMCs. The proposed approach determines the AC and DC side impedances of MMCs controlled by power and DC voltage control based on the system-level parameters.
- The effectiveness of using several smaller ANN models rather than a single ANN model over the entire frequency range in predicting impedance responses is demonstrated. The proposed transfer learning framework is validated, demonstrating its superiority over traditional ANN methods, particularly in scenarios where manufacturers keep certain converter parameters confidential.

The rest of the paper is organized as follows: Section II provides the overall framework of the proposed transfer learning-based impedance identification. Section III presents the results and discussions, and Section IV concludes the paper.

Notation: Vectors are denoted by using lowercase bold identifiers, such as $\boldsymbol{x}$, and matrices by uppercase bold identifiers, such as $\boldsymbol{X}$. The operator $\circ$ refers to the Hadamard product. $\boldsymbol{I}_n$ is the representation of an $n \times n$ identity matrix, whereas $\boldsymbol{J}_2 = \begin{bmatrix} 0 & 1 \\ -1 & 0 \end{bmatrix}$ and $\boldsymbol{J}_3 = \begin{bmatrix} 0 & 1 & 0 \\ -1 & 0 & 0 \\ 0 & 0 & 0 \end{bmatrix}$. The Fourier transform variable s is defined as $s = j\omega$, where j is the imaginary unit $j = \sqrt{-1}$ and ω represents the angular frequency. The real and imaginary components of a complex number $x \in \mathbb{C}$ are denoted by the symbols $\Re\{x\}$ and $\Im\{x\}$, respectively.

Park's transformation, described in (1), converts three-phase voltages and currents from the abc frame to the rotating dqz frame.

$$\mathbf{P}_\omega(t) = \frac{2}{3}\begin{bmatrix} \cos(\omega t) & \cos(\omega t - \frac{2\pi}{3}) & \cos(\omega t - \frac{4\pi}{3}) \\ \sin(\omega t) & \sin(\omega t - \frac{2\pi}{3}) & \sin(\omega t - \frac{4\pi}{3}) \\ \frac{1}{2} & \frac{1}{2} & \frac{1}{2} \end{bmatrix} \quad (1)$$

The inverse Park's transformation is defined as stated in (2).

$$\mathbf{P}_\omega^{-1}(t) = \frac{3}{2}\mathbf{P}_\omega^T(t) + \frac{1}{2}\begin{bmatrix} 0 & 0 & 1 \\ 0 & 0 & 1 \\ 0 & 0 & 1 \end{bmatrix} \quad (2)$$

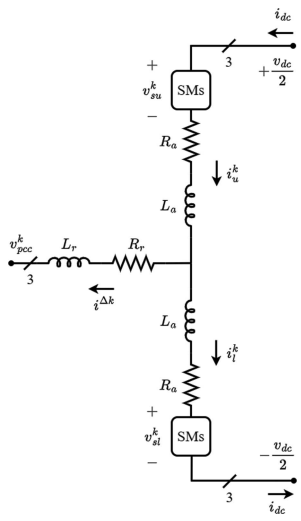

Fig. 1. Basic per-phase ($k \in \{a, b, c\}$) MMC topology consisting of submodules (SMs), equivalent arm resistance (R_{arm}) and inductance (L_{arm}).

II. Transfer Learning Framework for MMC Impedance Characterization

This section describes a transfer learning-based framework aimed at minimizing dependency on measured or simulated impedance data. Initially, the LTI model that facilitates the computation of the MMC's impedance characteristics and serves as a foundation for pre-training the ANN model is elaborated. Following this, the methodology for conducting simulations to measure impedance using real-time RTDS® simulators, which are capable of efficiently simulating complex converter systems, is described. Finally, the neural network training procedure and the proposed transfer learning methodology are outlined comprehensively.

A. LTI Model

The LTI model presented in [10] has been extended to include measurement filters that are present in the practical converters.

1) MMC Dynamics: The detailed dynamics of the converter model are presented using the procedure developed in [10], [22], [23], [24], [25]. Fig. 1 shows a single-phase architecture for a three-phase MMC, with all variables defined for all the phases, $k \in \{a, b, c\}$. The submodules are represented by an averaged equivalent model, allowing the voltages and currents in the upper and lower arms to be described by (3).

$$v_{su,l}^k = m_{u,l}^k v_{cu,l}^k \qquad i_{su,l}^k = m_{u,l}^k i_{u,l}^k \tag{3}$$

where $m_{u,l}^k$ are the corresponding upper and lower arm insertion indices.

The $\Sigma - \Delta$ nomenclature can be used to represent the variables in the upper and lower arms [22] as stated in (4).

$$i^{\Delta k} = i_u^k - i_l^k \qquad i^{\Sigma k} = \frac{i_u^k + i_l^k}{2} \tag{4a}$$

$$v_c^{\Delta k} = \frac{v_{cu}^k - v_{cl}^k}{2} \qquad v_c^{\Sigma k} = \frac{v_{cu}^k + v_{cl}^k}{2} \tag{4b}$$

$$m^{\Delta k} = m_u^k - m_l^k \qquad m^{\Sigma k} = m_u^k + m_l^k \tag{4c}$$

$$v_s^{\Delta k} = \frac{-v_{su}^k + v_{sl}^k}{2} = -\frac{m^{\Delta k} v_c^{\Sigma k} + m^{\Sigma k} v_c^{\Delta k}}{2} \tag{4d}$$

$$v_s^{\Sigma k} = \frac{v_{su}^k + v_{sl}^k}{2} = \frac{m^{\Sigma k} v_c^{\Sigma k} + m^{\Delta k} v_c^{\Delta k}}{2} \tag{4e}$$

The differential equations describing the dynamic behavior of the MMC can be derived by using the variables stated in (4).

$$\dot{\boldsymbol{i}}^{\Delta dq} = \frac{\boldsymbol{v}_s^{\Delta dq} - (\omega L_t \boldsymbol{J}_2 + R_t \boldsymbol{I}_2)\boldsymbol{i}^{\Delta dq} - \boldsymbol{v}_{pcc}^{dq}}{L_t} \tag{5a}$$

$$\dot{\boldsymbol{i}}^{\Sigma dq} = -\frac{\boldsymbol{v}_s^{\Sigma dq} + (R_a \boldsymbol{I}_2 - 2\omega L_a \boldsymbol{J}_2)\boldsymbol{i}^{\Sigma dq}}{L_a} \tag{5b}$$

$$\dot{i}^{\Sigma z} = \frac{v_{dc}}{2L_a} - \frac{v_s^{\Sigma z} + R_a i^{\Sigma z}}{L_a} \tag{5c}$$

$$\dot{\boldsymbol{v}}_c^{\Delta dq} = \frac{N}{2C}\boldsymbol{i}_s^{\Delta dq} - \omega \boldsymbol{J}_2 \boldsymbol{v}_c^{\Delta dq} \tag{5d}$$

$$\dot{\boldsymbol{v}}_c^{\Delta Zdq} = -\frac{N}{8C}\Psi - 3\omega \boldsymbol{J}_2 \boldsymbol{v}_c^{\Delta Zdq} \tag{5e}$$

$$\dot{\boldsymbol{v}}_c^{\Sigma dqz} = \frac{N}{2C}\boldsymbol{i}_s^{\Sigma dqz} + 2\omega \boldsymbol{J}_3 \boldsymbol{v}_c^{\Sigma dqz} \tag{5f}$$

$$\dot{v}_{dc} = \frac{1}{C_{dc}}\left(i_{dc} - 3i^{\Sigma z}\right) \tag{5g}$$

where,

$$\boldsymbol{i}_s^{\Delta dq} = \boldsymbol{P}_\omega(t)\left(\boldsymbol{P}_{-2\omega}^{-1}(t)\boldsymbol{m}_{\tau_d}^{\Sigma dqz} \circ \frac{\boldsymbol{P}_\omega^{-1}(t)\boldsymbol{i}^{\Delta dqz}}{2} + \boldsymbol{P}_\omega^{-1}(t)\boldsymbol{m}_{\tau_d}^{\Delta dqZ} \circ \boldsymbol{P}_{-2\omega}^{-1}(t)\boldsymbol{i}^{\Sigma dqz}\right)$$

$$\boldsymbol{i}_s^{\Sigma dqz} = \boldsymbol{P}_{-2\omega}(t)\left(\boldsymbol{P}_{-2\omega}^{-1}(t)\boldsymbol{m}_{\tau_d}^{\Sigma dqz} \circ \boldsymbol{P}_{-2\omega}^{-1}(t)\boldsymbol{i}^{\Sigma dqz} + \boldsymbol{P}_\omega^{-1}(t)\boldsymbol{m}_{\tau_d}^{\Delta dqZ} \circ \boldsymbol{P}_\omega^{-1}(t)\frac{\boldsymbol{i}^{\Delta dqz}}{2}\right)$$

$$\boldsymbol{v}_s^{\Delta dqz} = -\frac{\boldsymbol{P}_\omega}{2}(t)\left(\boldsymbol{P}_\omega^{-1}(t)\boldsymbol{m}_{\tau_d}^{\Delta dqZ} \circ \boldsymbol{P}_{-2\omega}^{-1}(t)\boldsymbol{v}_c^{\Sigma dqz} + \boldsymbol{P}_{-2\omega}^{-1}(t)\boldsymbol{m}_{\tau_d}^{\Sigma dqz} \circ \boldsymbol{P}_\omega^{-1}(t)\boldsymbol{v}_c^{\Delta dqz}\right)$$

$$\boldsymbol{v}_s^{\Sigma} = \frac{\boldsymbol{P}_{-2\omega}}{2}(t)\left(\boldsymbol{P}_\omega^{-1}(t)\boldsymbol{m}_{\tau_d}^{\Delta dqZ} \circ \boldsymbol{P}_\omega^{-1}(t)\boldsymbol{v}_c^{\Delta dqz} + \boldsymbol{P}_{-2\omega}^{-1}(t)\boldsymbol{m}_{\tau_d}^{\Sigma dqz} \circ \boldsymbol{P}_{-2\omega}^{-1}(t)\boldsymbol{v}_c^{\Sigma dqz}\right)$$

$$\Psi = \begin{bmatrix} i^{\Delta d} m_{\tau_d}^{\Sigma d} + 2i^{\Sigma d} m_{\tau_d}^{\Delta d} + i^{\Delta q} m_{\tau_d}^{\Sigma q} + 2i^{\Sigma q} m_{\tau_d}^{\Delta q} + 4i^{\Sigma z} m_{\tau_d}^{\Delta Zd} \\ i^{\Delta q} m_{\tau_d}^{\Sigma d} + 2i^{\Sigma d} m_{\tau_d}^{\Delta q} - i^{\Delta d} m_{\tau_d}^{\Sigma q} - 2i^{\Sigma q} m_{\tau_d}^{\Delta d} + 4i^{\Sigma z} m_{\tau_d}^{\Delta Zq} \end{bmatrix}$$

N represents the number of sub-modules, C is the sub-module capacitance, R_a and L_a are the arm resistance and inductance, $R_t = R_r + \frac{R_a}{2}$ and $L_t = L_r + \frac{L_a}{2}$ represent the equivalent AC resistance and inductance, and C_{dc} represents the equivalent DC side capacitance.

Eq. (5) represents variables using multiple dqz-frames by applying Park's transformation at different frequencies.

The Δ state variables are derived using the angular frequency components ω and 3ω, whereas the Σ variables use -2ω components [22]. The insertion indices $\boldsymbol{m} = \begin{bmatrix} \boldsymbol{m}^{\Delta dq} & \boldsymbol{m}^{\Delta Zdq} & \boldsymbol{m}^{\Sigma dqz} \end{bmatrix}^T$ are obtained as stated in (6).

$$\boldsymbol{m} = \frac{2}{v_{dc}} \begin{bmatrix} -\boldsymbol{v}_{s,ref}^{\Delta dqZ} \\ \boldsymbol{v}_{s,ref}^{\Sigma dqz} \end{bmatrix} \tag{6}$$

2) Time Delays: The MMC's impedance characteristics are highly susceptible to time delays (computational time delay, sampling delay, modulation delay, etc.) in the system, particularly in the low (10–100Hz) and high (several kHz) frequency ranges [26]. Therefore, these time delays must be considered during the modeling of the impedances. For simplicity, all time delays within the control architecture are consolidated into a single delay, based on the assumption that this aggregated delay can effectively represent the impact of the computational time delay on the impedance characteristics [10].

The time delay (τ_d) can be expressed as a rational transfer function using the Padé approximation stated in (7), where m and n are the numerator and denominator approximation orders, respectively [10], [27].

$$\boldsymbol{T}_{delay} = e^{-s\tau_d} \approx \frac{b_0 + b_1(\tau_d s)^1 + \cdots + b_m(\tau_d s)^m}{a_0 + a_1(\tau_d s)^1 + \cdots + a_n(\tau_d s)^n} \tag{7}$$

The rational transfer function approximation is then converted into the state-space form [27] with inputs $\begin{bmatrix} \boldsymbol{m}^{\Delta dq} & \boldsymbol{m}^{\Sigma dqz} \end{bmatrix}^T$, the insertion indices obtained from the controller outputs as given in (6), and the outputs $\begin{bmatrix} \boldsymbol{m}_{\tau_d}^{\Delta dqz} & \boldsymbol{m}_{\tau_d}^{\Sigma dqz} \end{bmatrix}^T$, the insertion indices which are used in the differential equations given in (5). A third-order ($m = n = 3$) approximation is used in this study because it accurately represents the impact of computational delay up to the 1kHz frequency range.

3) Controller Dynamics: The voltage references in (6) are obtained as an output of the controllers and the 13 differential equations stated in (5). The controllers can specify the voltage references, but by default, all voltage reference values are set to zero, except for $v_{c,ref}^z$, which is set to $\frac{v_{dc}}{2}$. When the controller specifies the voltage references, additional differential equations are required to represent the proportional integral (PI) controllers in the dqz frames [10], [22], [28].

The primary (inner) and secondary (outer) controllers that constitute the framework of the MMC control architecture are shown in Fig. 2(a). DC voltage control, active power control, and reactive power control act as the outer controllers, whereas output current control (OCC), and circulating current control (CCC) act as the inner controllers. Using the PI structure illustrated in Fig. 2(c), each controller and the PLL, shown in Fig. 2(b), can be defined using a set of differential equations provided in (8).

$$\dot{\xi} = \text{Ref.} - \text{Meas.} \tag{8a}$$

$$\text{Out} = K_P(\text{Ref.} - \text{Meas.}) + K_I\xi \tag{8b}$$

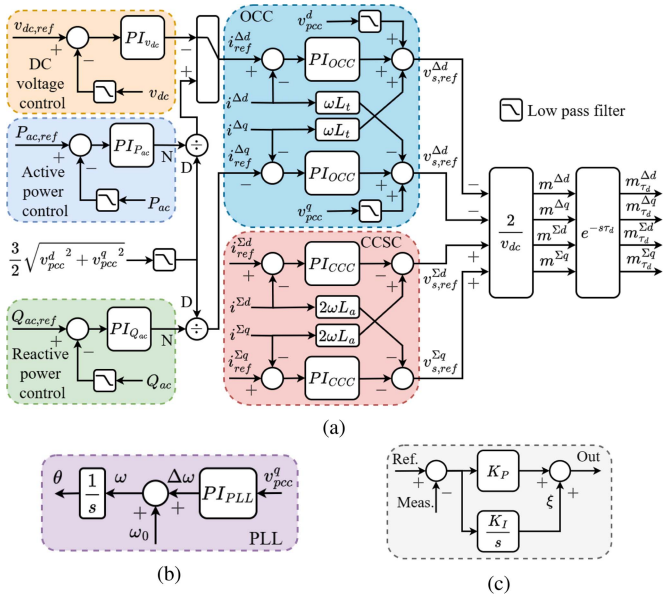

Fig. 2. MMC control architecture consisting of (a) inner controllers, outer controllers and time delay, (b) PLL, and (c) generic PI structure.

4) Measurement Filters: Filtering measured signals is often required for stable operation of the controllers in order to eliminate noise and correctly track changes in control variables. Filters also improve system stability by reducing undesirable high-frequency oscillations, resulting in more reliable and precise control. However, each filter in the system has a considerable effect on the converter's impedance characteristics. As a result, these filters must be considered during modeling.

Measurement filters can be modeled as first- or second-order low-pass filters, depending on the variable they govern. Commonly filtered variables in the MMC control structure are marked in Fig. 2(a). The variables v_{pcc}^{dq} in the OCC are filtered out using a first-order low-pass filter utilizing (9) to obtain filtered voltages $v_{pcc,filt}^{dq}$.

$$\dot{\xi}^{filt} = -\frac{1}{T_{filt}}\xi^{filt} + v_{pcc}^{dq} \tag{9a}$$

$$v_{pcc,filt}^{dq} = \frac{1}{T_{filt}}\xi^{filt} \tag{9b}$$

where T_{filt} represents the time constant of the first-order low-pass filter. The cut-off frequency for the filter is $f_{filt} = \frac{1}{T_{filt}}$.

Similarly, the measured input variables of outer controllers such as P_{ac}, Q_{ac}, and v_{dc} are subjected to second-order low-pass filters, which can be represented using (10).

$$\dot{\xi}_1^{filt} = -\omega_{filt}^2\xi_2^{filt} - 2\zeta\omega_{filt}\xi_1^{filt} + x \tag{10a}$$

$$\dot{\xi}_2^{filt} = \xi_1^{filt} \tag{10b}$$

$$x_{filt} = \omega_{filt}^2\xi_2^{filt} \tag{10c}$$

where x represents the input variables P_{ac}, Q_{ac}, and v_{dc}, x_{filt} represents the corresponding filtered variables $P_{ac,filt}$, $Q_{ac,filt}$,

and $v_{dc,filt}$, respectively, ω_{filt} is the filter's natural frequency, and ζ is the damping factor.

5) Operating Point: A power flow or steady-state simulation can be used to determine the operating point of the converter [10]. Using this approach, the following parameters are determined: DC voltage magnitude V_{dc}, active power at the DC terminal P_{dc} (flowing from the AC side to the DC side), AC voltage magnitude and phase V_{ac} and θ, respectively, active power at the AC terminal P_{ac} (flowing from the AC side to the DC side), and reactive power at the AC terminal Q_{ac} (flowing from the AC side to the DC side). The converter's reference values are then obtained using the values for the AC and DC voltages and powers as given by,

$$v_{dc,ref} = V_{dc}$$

$$v_{pcc}^{d} = V_{ac}\cos(\theta) \qquad v_{pcc}^{q} = -V_{ac}\sin(\theta)$$

$$P_{ac,ref} = -P \qquad Q_{ac,ref} = Q$$

$$i_{ref}^{\Delta d} = \frac{2(v_{pcc}^{d}P + v_{pcc}^{q}Q)}{3({v_{pcc}^{d}}^2 + {v_{pcc}^{q}}^2)} \qquad i_{ref}^{\Delta q} = \frac{2(v_{pcc}^{q}P - v_{pcc}^{d}Q)}{3({v_{pcc}^{d}}^2 + {v_{pcc}^{q}}^2)}$$

6) Steady State Solution and Admittance Model: After modeling all the necessary differential equations for the MMC and controllers, an equilibrium point is obtained using the Julia package NLsolve [29], which represents the solution to these differential equations. Further, the system of differential equations is represented as a multi-input multi-output (MIMO) system in a linearized form, as given in (12).

$$\dot{\boldsymbol{x}}(t) = \boldsymbol{A}_{MMC}\boldsymbol{x}(t) + \boldsymbol{B}_{MMC}\boldsymbol{u}(t) \tag{12a}$$

$$\boldsymbol{y}(t) = \boldsymbol{C}_{MMC}\boldsymbol{x}(t) + \boldsymbol{D}_{MMC}\boldsymbol{u}(t) \tag{12b}$$

where $\boldsymbol{x}$ represents all the state variables given in (5) and additional state variables introduced by the applied controllers, $\boldsymbol{u} = [v_{dc} \quad v_{pcc}^{d} \quad v_{pcc}^{q}]^T$ is the input vector, and $\boldsymbol{y} = [i_{dc} \quad i^{\Delta d} \quad i^{\Delta q}]^T$ is the output. When the MMC controls the DC voltage, the input and output vectors are redefined as $\boldsymbol{u} = [i_{dc} \quad v_{pcc}^{d} \quad v_{pcc}^{q}]^T$ and $\boldsymbol{y} = [v_{dc} \quad i^{\Delta d} \quad i^{\Delta q}]^T$.

The associated matrices $\boldsymbol{A}_{MMC}$, $\boldsymbol{B}_{MMC}$, $\boldsymbol{C}_{MMC}$, and $\boldsymbol{D}_{MMC}$, expressed in (12), are determined as Jacobians around the aforementioned equilibrium point using the Julia package ForwardDiff [30]. Using the Laplace transform, the equations in (12) can be transformed into a MIMO transfer function.

$$\boldsymbol{Y}_{MMC}(s) = \boldsymbol{C}_{MMC}(s\boldsymbol{I} - \boldsymbol{A}_{MMC})^{-1}\boldsymbol{B}_{MMC} + \boldsymbol{D}_{MMC} \tag{13}$$

where $\boldsymbol{Y}_{MMC}(s)$ represents the admittance matrix of the system and is given by (14).

$$\boldsymbol{Y}_{MMC}(s) = \begin{bmatrix} Y_{1,1}(s) & Y_{1,2}(s) & Y_{1,3}(s) \\ Y_{2,1}(s) & Y_{2,2}(s) & Y_{2,3}(s) \\ Y_{3,1}(s) & Y_{3,2}(s) & Y_{3,3}(s) \end{bmatrix} \tag{14}$$

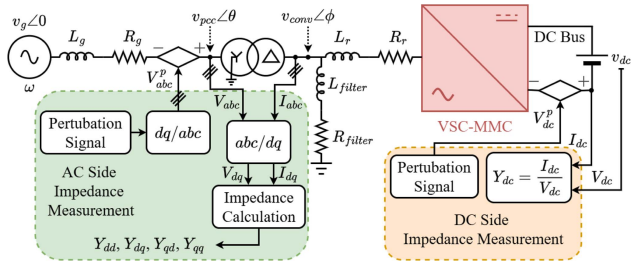

Fig. 3. AC and DC side impedance measurement configuration.

By separating the AC and DC side impedances from Y_{MMC}, (15) is obtained.

$$\boldsymbol{Y}_{ac}(s) = \begin{bmatrix} Y_{dd}(s) & Y_{dq}(s) \\ Y_{qd}(s) & Y_{qq}(s) \end{bmatrix} = \begin{bmatrix} -Y_{2,2}(s) & Y_{2,3}(s) \\ Y_{3,2}(s) & -Y_{3,3}(s) \end{bmatrix} \tag{15a}$$

$$Y_{dc}(s) = Y_{1,1}(s) \tag{15b}$$

where $\boldsymbol{Y}_{ac}(s)$ represents the AC side impedance in the dq frame and $Y_{dc}(s)$ represents the DC side impedance.

However, when the MMC controls the DC voltage, a subsequent step is needed after computing $\boldsymbol{Y}_{MMC}(s)$ using (13). This step involves transforming the positions of $v_{dc}(s)$ and $i_{dc}(s)$ and removing the effect of the capacitance C_{dc}. The DC side impedance can then be calculated using (16).

$$Y_{dc}(s) = 2\left(\frac{1}{Y_{1,1}(s)} - sC_{dc}\right) \tag{16}$$

B. Impedance Measurement

The system diagram of a grid-connected MMC in monopolar configuration which is used for the impedance measurement is shown in Fig. 3. For simplicity, the AC and DC side impedances are depicted together; however, in actual simulations, they need to be measured independently. A similar configuration is replicated in the RSCAD simulation running on real-time RTDS® simulators. The MMC and its control are executed on hardware GTFPGA modules within the RTDS® simulator, operating in real-time synchronization with the simulator. The '*rtds_ss_MMC_GMMX_FPGA_eb*' model is utilized for this implementation [31], [32]. To handle computational demands, each leg of the MMC is simulated on a separate GTFPGA module, with two additional modules dedicated to capacitor voltage balancing and the lower-level controller. These modules communicate submodule capacitor voltage values and firing sequences via two full-duplex optical fibers connected to the MMC's lower-level controller. Consequently, the voltage source converter is implemented using a total of five GTFPGA modules. This setup is utilized for conducting the impedance measurements.

The basic principle for measuring both AC and DC side impedances is similar. The initial step is to bring the system to a steady state at a specific operating point. Then, a perturbation voltage V^p is injected into the system, and the resulting voltages and currents at the respective terminals are measured. The

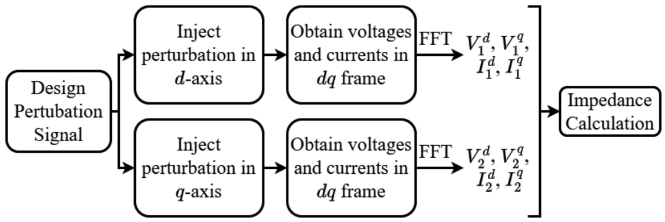

Fig. 4. Steps performed for measuring AC side impedance in dq frame.

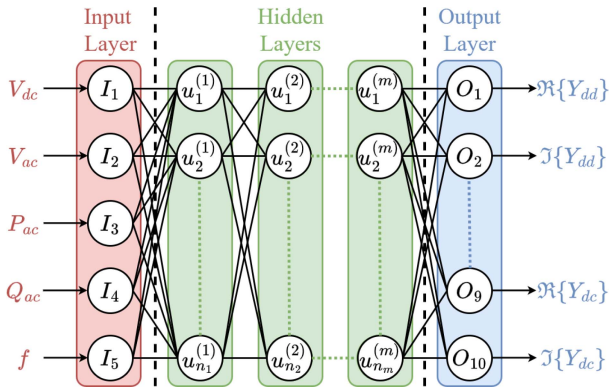

Fig. 5. Structure of a typical ANN with the inputs being the converter operating point and the outputs being the admittances.

detailed procedure for measuring and computing the AC side dq impedance is given in Fig. 4. Because this study only focuses on the impedances of MMCs, R_g and L_g are set to zero. The '*Harmonic Scan*' component in RSCAD is used to inject perturbation signals and perform the appropriate post-processing steps to acquire impedance values [33], [34], [35].

C. Neural Network Training

A typical ANN structure used for this study is shown in Fig. 5. It consists of one input layer with five neurons, representing the MMC's operating point and frequency (V_{dc}, V_{ac}, P_{ac}, Q_{ac}, and f); m hidden layers with u_{n_1}, u_{n_2}, $\cdots$, u_{n_m} neurons; and one output layer with ten neurons, representing the AC and DC side admittances of the converter ($\Re\{Y_{dd}\}$, $\Im\{Y_{dd}\}$, $\Re\{Y_{dq}\}$, $\Im\{Y_{dq}\}$, $\Re\{Y_{qd}\}$, $\Im\{Y_{qd}\}$, $\Re\{Y_{qq}\}$, $\Im\{Y_{qq}\}$, $\Re\{Y_{dc}\}$, and $\Im\{Y_{dc}\}$). Each neuron in the ANN, specifically in the ith hidden layer, is modeled using (17).

$$\boldsymbol{u}^{(i)} = a^{(i)}\{\boldsymbol{W}^{(i)}\boldsymbol{u}^{(i-1)} + \boldsymbol{b}^{(i)}\} \tag{17}$$

where $a^{(i)}$ denotes the ith hidden layer's activation function, and $\boldsymbol{u}^{(i)}$, $\boldsymbol{W}^{(i)}$, and $\boldsymbol{b}^{(i)}$ denote the neuron values, weights, and biases in the ith hidden layer. These parameters are provided by (18).

$$\boldsymbol{u}^{(i)} = \begin{bmatrix} u_1^{(i)} & u_2^{(i)} & \cdots & u_{n_i}^{(i)} \end{bmatrix}^T \tag{18a}$$

$$\boldsymbol{W}^{(i)} = \begin{bmatrix} W_{1,1}^{(i)} & W_{1,2}^{(i)} & \cdots & W_{1,n_{i-1}}^{(i)} \\ W_{2,1}^{(i)} & W_{2,2}^{(i)} & \cdots & W_{2,n_{i-1}}^{(i)} \\ \vdots & \vdots & \ddots & \vdots \\ W_{n_i,1}^{(i)} & W_{n_i,2}^{(i)} & \cdots & W_{n_i,n_{i-1}}^{(i)} \end{bmatrix} \tag{18b}$$

$$\boldsymbol{b}^{(i)} = \begin{bmatrix} b_1^{(i)} & b_2^{(i)} & \cdots & b_{n_i}^{(i)} \end{bmatrix}^T \tag{18c}$$

The neuron values for the first hidden layer and the output layer can be obtained from (17) using (19).

$$\boldsymbol{u}^{(1)} = a^{(1)}\{\boldsymbol{W}^{(1)}\boldsymbol{I} + \boldsymbol{b}^{(1)}\} \tag{19a}$$

$$\boldsymbol{O} = \boldsymbol{W}^{(m+1)}\boldsymbol{u}^{(m)} + \boldsymbol{b}^{(m+1)} \tag{19b}$$

where $\boldsymbol{I} = \begin{bmatrix} I_1 & I_2 & \cdots & I_5 \end{bmatrix}^T$ represent the 5 input values, and $\boldsymbol{O} = \begin{bmatrix} O_1 & O_2 & \cdots & O_{10} \end{bmatrix}^T$ represent the 10 output values, and

$$\boldsymbol{W}^{(m+1)} = \begin{bmatrix} W_{1,1}^{(m+1)} & W_{1,2}^{(m+1)} & \cdots & W_{1,n_m}^{(m+1)} \\ W_{2,1}^{(m+1)} & W_{2,2}^{(m+1)} & \cdots & W_{2,n_m}^{(m+1)} \\ \vdots & \vdots & \ddots & \vdots \\ W_{10,1}^{(m+1)} & W_{10,2}^{(m+1)} & \cdots & W_{10,n_m}^{(m+1)} \end{bmatrix} \tag{20a}$$

$$\boldsymbol{b}^{(m+1)} = \begin{bmatrix} b_1^{(m+1)} & b_2^{(m+1)} & \cdots & b_{10}^{(m+1)} \end{bmatrix}^T \tag{20b}$$

The performance of the ANN with different configurations of neurons in each hidden layer is systematically evaluated using techniques such as grid search or random search, aiming to identify the optimal architecture that maximizes predictive accuracy while avoiding overfitting. For simplicity, the number of neurons in each hidden layer is kept equal. Subsequently, the Optuna framework [36] is employed to optimize the hyperparameters based on the coefficient of determination (R^2) value for each model. Here, the kernel regularization parameter for the neurons, the activation function in each hidden layer, and the learning rate of the Adam optimizer are tuned through 50 trials. This optimization process helps avoid overfitting and achieves optimal performance on the training, validation, and test sets.

The ANN model described above undergoes a comprehensive training process. The overall dataset is initially divided into three parts: 70% for training, 15% for validation, and 15% for testing. During each epoch of the training process, the training and validation sets are randomly shuffled to ensure that every item has an equal chance of being used for training. This shuffling process enhances the robustness and generalization capability of the model.

Next, the ANN is trained using the back-propagation algorithm, which employs the mean squared error (MSE) loss function and the mean absolute error (MAE) metric to evaluate the difference between the ANN's predictions and the provided admittance data. The primary objective of the training process is to minimize the MSE by updating the weights and biases of each neuron using the Adam optimizer. The Adam optimizer is chosen for its efficiency in handling large datasets and its

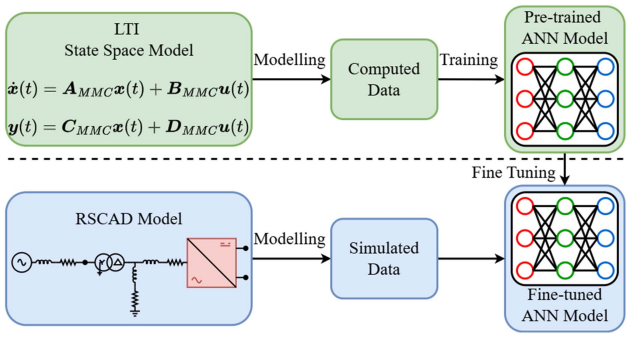

Fig. 6. Proposed transfer learning-based framework for impedance characterization of MMCs.

adaptive learning rate capabilities, which make it suitable for this complex modeling task.

Finally, the trained ANN model is evaluated using the test set. Its performance is assessed using the MAE plots. If a n prediction vector is constructed from a sample of n data points, then the MSE, MAE, and R^2 values can be given by,

$$MSE = \frac{1}{n}\sum_{i=1}^{n}(y_i - \hat{y}_i)^2 \tag{21a}$$

$$MAE = \frac{1}{n}\sum_{i=1}^{n}(y_i - \hat{y}_i) \tag{21b}$$

$$R^2 = 1 - \frac{\sum_{i=1}^{n}(y_i - \hat{y}_i)^2}{\sum_{i=1}^{n}\left(y_i - \frac{1}{n}\sum_{i=1}^{n} y_i\right)^2} \tag{21c}$$

where, y_i is the ith data point value in the observed vector, and $\hat{y}_i$ is the ith data point value in the prediction vector. An R^2 value close to 1 indicates that the model accurately captures the variance in the admittance data.

By following this detailed and systematic approach, the ANN model is effectively trained to predict the AC and DC side admittances of the MMC, enabling a reliable and efficient transfer learning framework for impedance characterization.

D. Transfer Learning

Conventional ANN models typically demand extensive datasets to accurately estimate MMC impedances. However, obtaining AC and DC side impedance responses through separate simulations consumes a considerable amount of time, particularly when generating impedance data across a wide spectrum of operating points. In response to this challenge, this paper proposes a transfer learning framework, illustrated in Fig. 6, for accurate estimation of MMC impedances. The central concept of this framework is to leverage a diverse dataset encompassing a broad array of operating points generated using the LTI model and subsequently train a neural network. Following this, detailed simulations in RSCAD are employed to conduct impedance measurements for a smaller subset of operating points. Finally, the pre-trained ANN model undergoes fine-tuning using the simulated data to achieve optimal accuracy.

The process of collecting converter admittances involves iterative steps using both the LTI model defined in Section II-A and the impedance measurement procedure detailed in Section II-B. This iterative approach entails sweeping through a series of operating points specified according to reasonable power system operation criteria [37]. For each control mode, two datasets are generated: computed data and simulated data. The computed data corresponds to values computed based on the LTI model, whereas simulated data is obtained from real-time simulations. Both datasets are constructed similarly, with the operating ranges of the converters normalized on a per-unit basis: $V_{dc} \in [0.9, 1.1]$, $V_{ac} \in [0.9, 1.1]$, $P_{ac} \in [-1, 1]$, and $Q_{ac} \in [-1, 1]$.

TABLE I
RATED VALUES OF THE TEST CONVERTER [21]

Symbol	Value	Symbol	Value
S_{rated}	800 MVA	ω	$2\pi 50$ rad/s
N	200	C	10 mF
R_a	0 Ω	L_a	29 mH
R_r	0.363 Ω	L_r	35 mH
$v_{conv,L-L\ rated}$	220 kV	$v_{dc,P-P\ rated}$	400 kV
$v_{pcc,L-L\ rated}$	380 kV	R_g, L_g	0

TABLE II
CONTROL PARAMETERS OF THE TEST CONVERTER [21]

Type	Symbol	Value	Symbol	Value
PLL	K_P^{PLL}	300 p.u.	K_I^{PLL}	200 p.u.
OCC control	$K_P^{\Delta dq}$	0.48 p.u.	$K_I^{\Delta dq}$	149 p.u.
CCC control	$K_P^{\Sigma dq}$	0.8 p.u.	$K_I^{\Sigma dq}$	100 p.u.
DC voltage control	K_P^{dc}	8 p.u.	K_I^{dc}	272 p.u.
Active power control	K_P^{P}	0 p.u.	K_I^{P}	33 p.u.
Reactive power control	K_P^{Q}	0 p.u.	K_I^{Q}	33 p.u.

TABLE III
MEASUREMENT FILTER PARAMETERS OF THE TEST CONVERTER [21]

Type	Symbol	Value	Symbol	Value
v_{pcc}^{dq} filter	$T_{v_{pcc}^{dq}}$	0.0909		
P_{ac} filter	$\zeta_{P_{ac}}$	0.7	$\omega_{P_{ac}}$	$2\pi 16$ rad/s
Q_{ac} filter	$\zeta_{Q_{ac}}$	0.7	$\omega_{Q_{ac}}$	$2\pi 16$ rad/s
v_{ac} filter	$\zeta_{v_{ac}}$	0.7	$\omega_{v_{ac}}$	$2\pi 16$ rad/s
v_{dc} filter	$\zeta_{v_{dc}}$	0.7	$\omega_{v_{dc}}$	$2\pi 1000$ rad/s

III. EXPERIMENTAL RESULTS

To validate the proposed transfer learning framework outlined in Section II, converter A1 from the CIGRE B4 DC grid test system is modeled similarly to the system diagram shown in Fig. 3 [21]. The rated values, control parameters, and filter parameters for the converter are stated in Tables I to III, respectively. For effective control of the MMC system in both power and DC voltage control modes, different modeling approaches are necessary. In power control mode simulation, the DC side is considered a rigid DC source with voltage v_{dc} [24]. Conversely, in DC voltage control mode, the DC side bus is represented as a variable DC voltage system with an ideal power source, where the DC voltage v_{dc} mirrors the dynamic state of the DC side capacitor C_{dc} [24]. The value of C_{dc} is set to 500 μF to ensure stable operating conditions across all operating points.

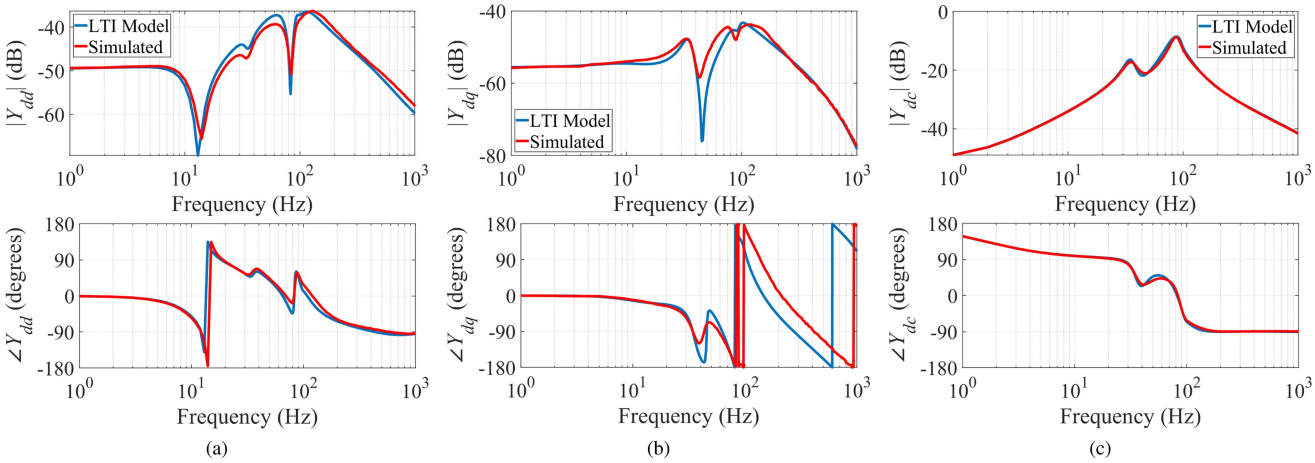

Fig. 7. Comparison of LTI model with simulated results for power controlled MMC.

TABLE IV
OPERATING POINT AND FREQUENCY STEPS IN SIMULATED AND COMPUTED DATASETS

Dataset	Parameter	Range	Step size
Simulated data	V_{dc}	[0.9, 1.1] p.u.	0.1 p.u.
	V_{ac}	[0.9, 1.1] p.u.	0.1 p.u.
	P_{ac}	[-1, 1] p.u.	0.4 p.u.
	Q_{ac}	[-1, 1] p.u.	0.3 p.u.
	f	[1,10] Hz	1 Hz
		[10, 100] Hz	3 Hz
		[100, 1000] Hz	30 Hz
Computed data	V_{dc}	[0.9, 1.1] p.u.	0.1 p.u.
	V_{ac}	[0.9, 1.1] p.u.	0.1 p.u.
	P_{ac}	[-1, 1] p.u.	0.2 p.u.
	Q_{ac}	[-1, 1] p.u.	0.2 p.u.
	f	[1,10] Hz	1 Hz
		[10, 100] Hz	1 Hz
		[100, 1000] Hz	10 Hz

The impedance measurement procedure is repeated multiple times to iteratively obtain the AC and DC side impedances of the converter for normalized operating points and frequency steps, as shown in Table IV. Similarly, the LTI model is used to generate a diverse dataset for the same operating points and frequency steps, taking into account a 600 μs computational time delay in the converter. Both datasets exclude operating points leading to overmodulation and overcurrent conditions, and separate datasets are obtained for each control mode. As a result, the final datasets consist of 7840 data points (112 operating points $\times$ 70 frequency points) in the simulated data and 383030 data points (437 operating points $\times$ 190 frequency points) in the computed data. When comparing the datasets with those from previous studies [12], [19], it becomes evident that the dataset size in this study is considerably larger. This increase in size is necessary due to the diversity in frequency steps, which is crucial for accurately capturing admittance trends and avoiding any omission of critical peaks, particularly in the case of MMCs. In contrast, [19] conducted measurements across only a single operating point variable, whereas this study accounts for multiple operating point variables. This broader consideration significantly increases the number of possible combinations, resulting in a more comprehensive set of admittance patterns.

Fig. 7 shows the admittance at a particular operating point ($V_{dc} = 1$ p.u., $V_{ac} = 1$ p.u., $P_{ac} = -0.6$ p.u., $Q_{ac} = 0.3$ p.u.) to compare the two datasets. The LTI model effectively captures the admittance characteristics, with only minor differences in the values across all variables. However, the phase values of the cross-coupling elements Y_{dq} and Y_{qd} exhibit slightly higher deviations. The admittance values generated by both the LTI model and the simulated model are closely aligned, so they effectively capture variations in admittance as operating point variables change. Additionally, as the computed data covers a broader range of operating points, Figs. 8 and 9 present a subset of the computed dataset for power control mode. To simplify the presentation, only 3 out of the 10 output admittance variables are plotted. However, the remaining variables exhibit similar behavior. For instance, changes in parameters similarly affect both the dd and qq admittances, as well as the dq and qd admittances. Additionally, the impact of parameter changes on the real parts is similar to their effect on the imaginary parts.

It is observed that the admittances Y_{dd} and Y_{qq} are primarily influenced by P_{ac}, while Y_{dq} and Y_{qd} are mainly dependent on Q_{ac}. In contrast, the admittance Y_{dc} varies with both P_{ac} and Q_{ac}. The relationship of the voltages V_{ac} and V_{dc} to the admittances is minor compared to that of P_{ac} and Q_{ac}. Similar variations are noted in DC voltage control datasets, except that the voltages V_{ac} and V_{dc} exhibit significant variation in relation to the admittance Y_{dc}.

A. When Converter is Controlled Using Power Control

After acquiring the necessary datasets, the proposed method is initially tested for an MMC operating in power control mode. Traditional methods from previous studies employ a single ANN model for the entire frequency range. However, the dependency of the admittances on the input variables varies with frequency. This subsection provides details on this approach and its testing, both when using a single ANN model for the entire frequency

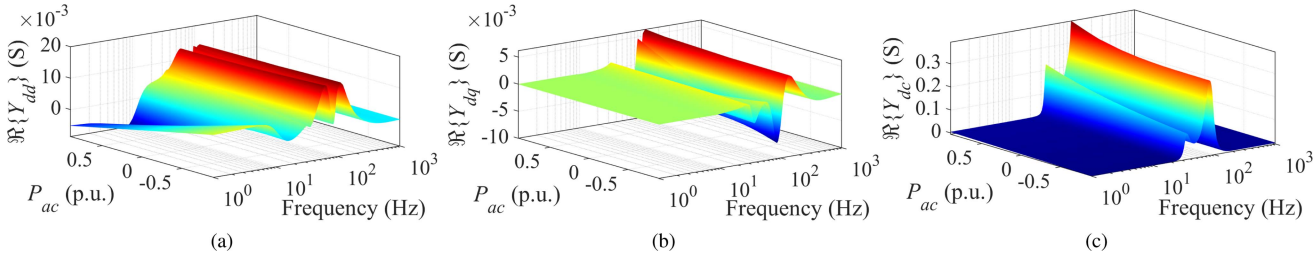

Fig. 8. Variation of (a) Y_{dd}, (b) Y_{dq}, and (c) Y_{dc} with respect to P_{ac} and f when $V_{ac} = 1$ p.u., $V_{dc} = 1$ p.u., and $Q_{ac} = 0$ p.u. and the MMC operates in power control mode.

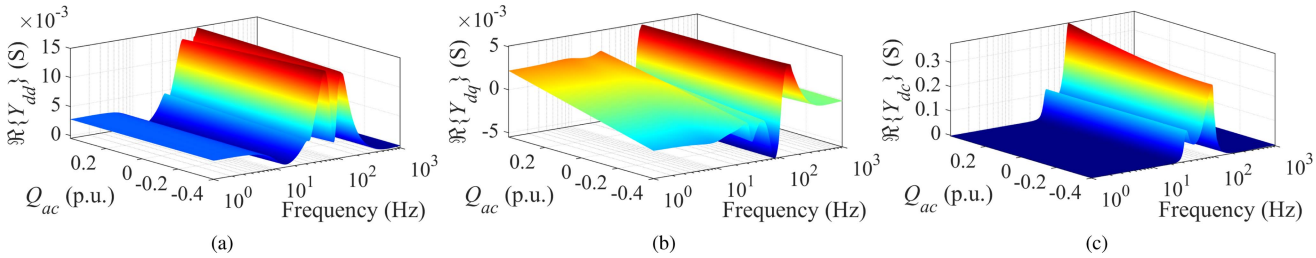

Fig. 9. Variation of (a) Y_{dd}, (b) Y_{dq}, and (c) Y_{dc} with respect to Q_{ac} and f when $V_{ac} = 1$ p.u., $V_{dc} = 1$ p.u., and $P_{ac} = -0.5$ p.u. and the MMC operates in power control mode.

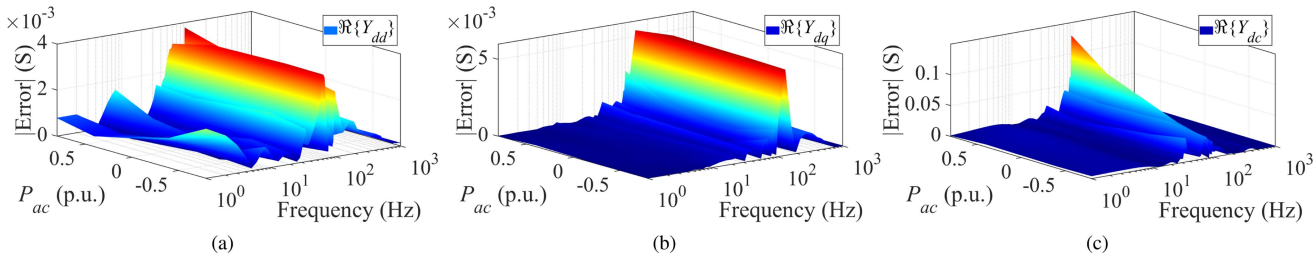

Fig. 10. Error between ANN trained using the LTI model and simulated data for (a) Y_{dd}, (b) Y_{dq}, and (c) Y_{dc} for a power controlled MMC.

range and when using separate models for different frequency ranges.

1) Single ANN Over the Whole Frequency Range: Initially, the entire frequency range is considered and trained using a single ANN model for power control mode. The neural network architecture for this purpose includes three hidden layers, each with 100 neurons, due to the complex nature of the admittances concerning frequency. First, the large neural network structure is pre-trained on the dataset obtained from the LTI model and then fine-tuned using the dataset obtained from EMT simulations. The batch size is set to 128 to ensure smooth loss gradients during training. The pre-trained model is used to predict the admittances for a set of test operating points. These points include all data points in the plane $V_{ac} = 1$ p.u., $V_{dc} = 1$ p.u., and $Q_{ac} = 0$ p.u., which are not considered in the training or validation set. The corresponding errors between the pre-trained model and the actual admittances obtained from EMT simulations in the same plane are plotted as depicted in Fig. 10. It can be observed that the pre-trained model significantly deviates from the actual admittance data generated using EMT simulations. This deviation is due to several types of non-linearities and non-modelable quantities, such as sampling error and the exact value of computational time delay, which are not considered in the LTI model. Therefore, the use of transfer learning and fine-tuning is required.

Finally, the errors between the models obtained using the conventional ANN method (trained solely with simulated data) and the actual admittances obtained from EMT simulations are depicted in Fig. 11. These are compared with the errors between the models obtained using transfer learning and the actual admittances obtained from EMT simulations, as shown in Fig. 12.

The errors in the conventional ANN method are higher (around 2 to 3 times) than those in the proposed method, as the model cannot generalize for unseen operating points and frequency steps due to limited data availability. This comparison shows that transfer learning-based models can achieve better performance and be generalized appropriately across all operating

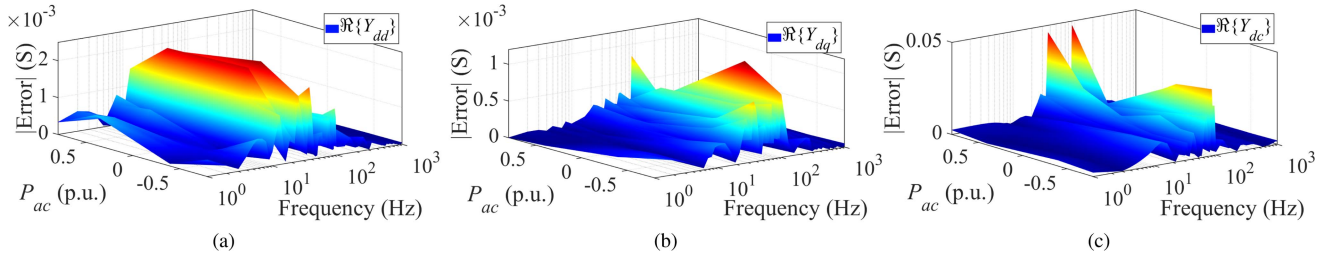

Fig. 11. Error between ANN trained on simulated data over the entire frequency range and a set of test operating points for (a) Y_{dd}, (b) Y_{dq}, and (c) Y_{dc} when the MMC operates in power control mode.

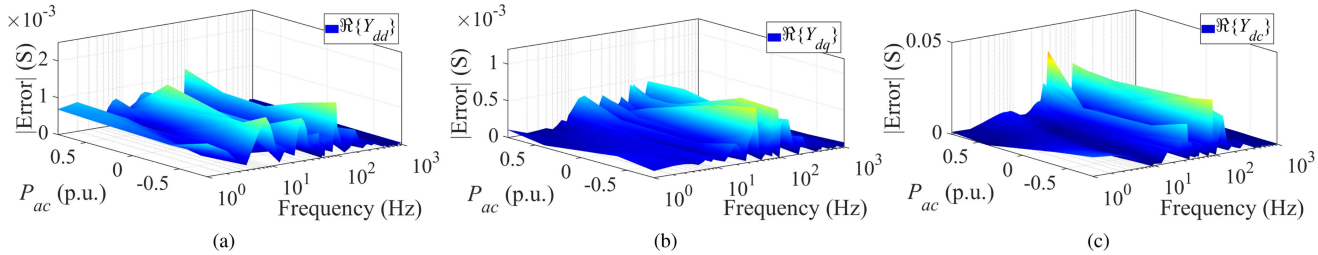

Fig. 12. Error between ANN trained using transfer learning over the entire frequency range and a set of test operating points for (a) Y_{dd}, (b) Y_{dq}, and (c) Y_{dc} when the MMC operates in power control mode.

points and frequency steps, even with limited simulation data availability.

2) Splitting Models Based on Frequency Range: Further analysis of the dataset reveals that admittances vary at different scales across certain frequency ranges. Additionally, the dependency of the admittances on the input variables changes with frequency. Admittances in the 1–10 Hz frequency range depend highly on active and reactive power. In the 10–100 Hz frequency range, admittances primarily depend not only on active and reactive power but also on frequency. Lastly, in the 100–1000 Hz frequency range, admittances are predominantly dependent on frequency, as depicted in Fig. 13. This conclusion is drawn from the analysis of correlation matrices for each frequency range, where the dependence of admittance parameters on input variables is assessed. As a result, it is evident that each frequency range exhibits a distinct dependency on the input variables, highlighting the varying impacts across different frequency ranges.

Leveraging the data dependency within each frequency range, separate ANN models are implemented to optimize the impedance identification process. Instead of using a single ANN model for the entire frequency range, smaller ANN architectures are utilized to estimate admittances within specific frequency ranges. Based on the non-linearity of the admittance values, 1, 3, and 2 hidden layers are implemented for the 1–10 Hz, 10–100 Hz, and 100–1000 Hz frequency ranges, respectively. Each hidden layer contains 50 neurons, while the batch size during training is set to 64.

For MMC controlled in power control mode, the error between the ANN trained using the proposed method by splitting models based on frequency range and the simulated data is depicted in Fig. 14. Comparing Figs. 12 and 14, it is evident that splitting models based on frequency range can reduce the error between the trained ANN model and the simulated data, resulting in a better fit. This method significantly improves accuracy, particularly in the low-frequency range of 1–10 Hz.

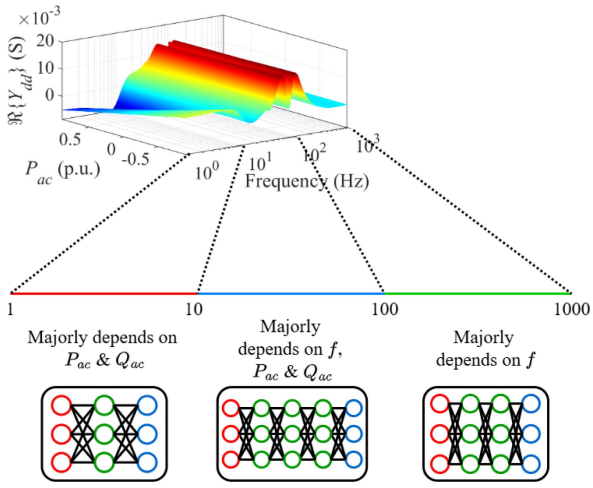

Fig. 13. Splitting frequency range and based on their dependencies.

B. When Converter is Controlled Using DC Voltage Control

Similar to the power-controlled MMC, the proposed method accurately estimates the admittances for the MMC controlled using a DC voltage controller. An important observation is demonstrated by setting the parameter C_{dc} to 600 μF in the LTI

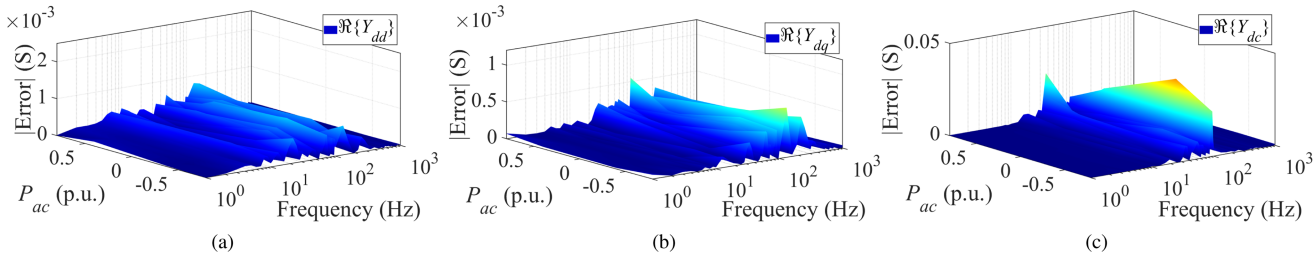

Fig. 14. Error between the ANN trained using transfer learning, with models split based on frequency range, and a set of test operating points for (a) Y_{dd}, (b) Y_{dq}, and (c) Y_{dc} when the MMC operates in power control mode.

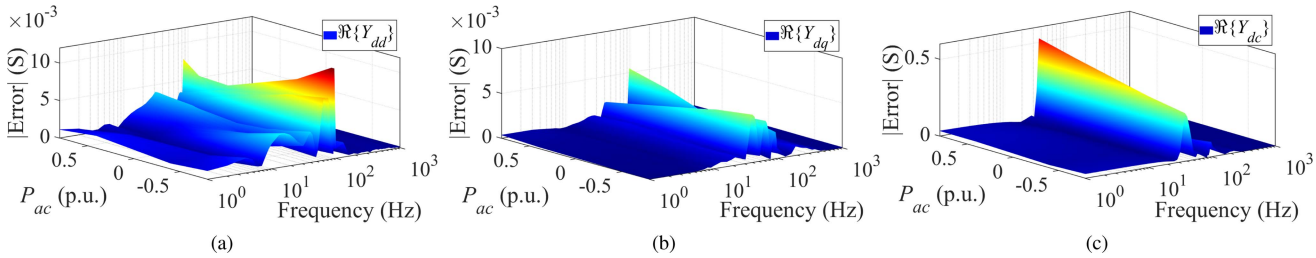

Fig. 15. Error between ANN trained on simulated data over the entire frequency range and a set of test operating points for (a) Y_{dd}, (b) Y_{dq}, and (c) Y_{dc} when the MMC operates in DC voltage control mode.

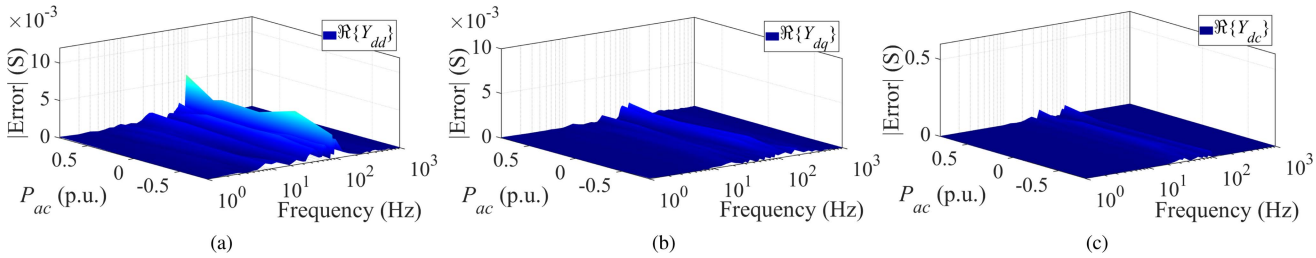

Fig. 16. Error between the ANN trained using transfer learning, with models split based on frequency range, and a set of test operating points for (a) Y_{dd}, (b) Y_{dq}, and (c) Y_{dc} when the MMC operates in DC voltage control mode.

model, contrasting with its value of 500 μF in the simulation model. Despite the slight variation in this parameter, which causes significant deviations in the admittances, the proposed method exhibits substantial accuracy compared to the conventional ANN approach. This is highlighted in the corresponding errors depicted in Figs. 15 and 16.

C. Transferability of Controllers

To facilitate transferability between different control diagrams, the model requires fine-tuning with impedance data specific to the new control strategy. This fine-tuning process is achievable within the proposed framework, allowing pre-trained ANN models to adapt to the unique impedance characteristics of the new control mode. By leveraging previously learned patterns, the model adjusts to variations introduced by different control loops and operating conditions. As a result, while the framework is robust and adaptable, practical implementation across various control diagrams requires additional data and fine-tuning to ensure accurate impedance predictions across a wide range of control strategies.

Figs. 17 and 18 presents the error plots when one controller's admittance characteristics are used for pre-training and the other's characteristics for fine-tuning. Comparing these results with those from the conventional ANN method in Figs. 11 and 15, it is evident that the model performs better, even when pre-trained with admittance values from a completely different dataset. However, the performance is still lower than when pre-trained using the same controller, as seen in Figs. 14 and 16. This discrepancy arises due to the significant differences in the datasets for both controllers. Therefore, although transferability is demonstrated, it is crucial to account for the deviations in the datasets when applying the proposed transfer learning methodology [38].

D. When Several Control Parameters are Unknown

In certain scenarios, manufacturers keep converter data confidential, making it impossible to accurately estimate impedance characteristics using the LTI model. However, the proposed transfer learning method allows for training the ANN model on

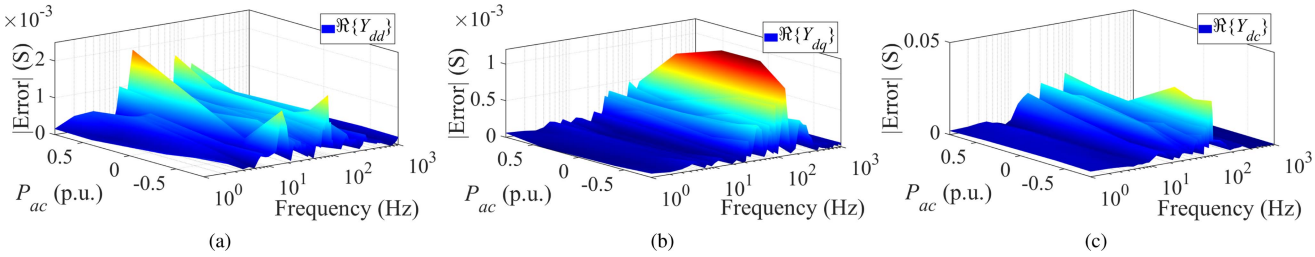

Fig. 17. Error between the ANN trained using transfer learning, with models split based on frequency range, and a set of test operating points for (a) Y_{dd}, (b) Y_{dq}, and (c) Y_{dc} when the MMC operates in power control mode. The ANN model is pre-trained using the LTI model having DC voltage control.

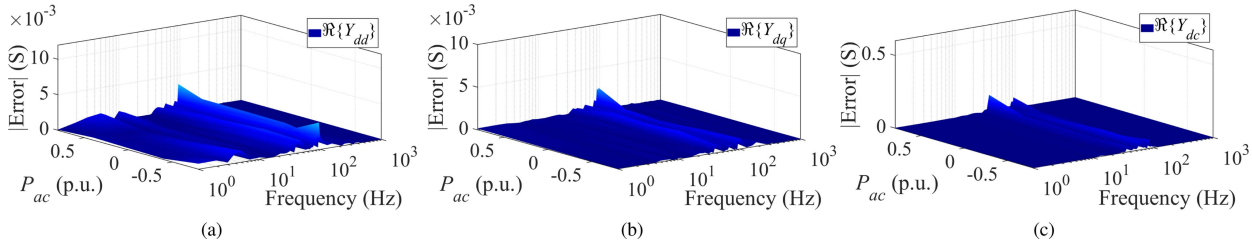

Fig. 18. Error between the ANN trained using transfer learning, with models split based on frequency range, and a set of test operating points for (a) Y_{dd}, (b) Y_{dq}, and (c) Y_{dc} when the MMC operates in DC voltage mode. The ANN model is pre-trained using the LTI model having power control.

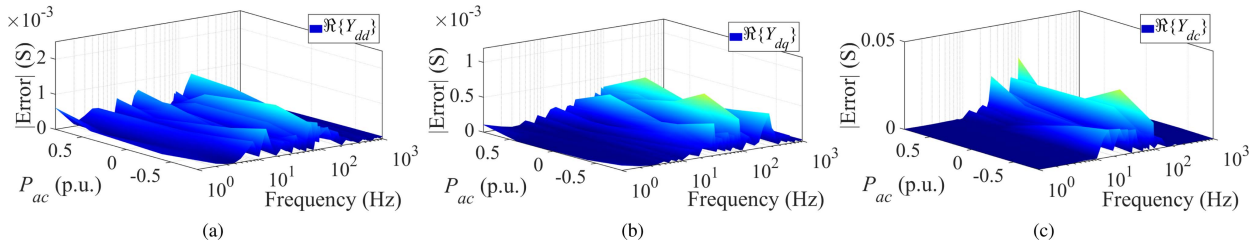

Fig. 19. Error between the ANN trained using transfer learning, with models split based on frequency range, and a set of test operating points for (a) Y_{dd}, (b) Y_{dq}, and (c) Y_{dc} when the MMC operates in power control mode. The ANN model is pre-trained using the LTI model with control parameters different from those in the simulation model.

a large dataset generated using the LTI model with slightly different parameters. This pre-trained model can then be fine-tuned using simulated data to achieve an accurate representation.

To further demonstrate the proposed method for such scenarios, the dataset generated using the LTI model for power control mode is obtained with a different set of control parameters compared to the simulated dataset. Specifically, the values of $K_P^{\Delta dq}$, $K_I^{\Delta dq}$, K_I^P, and K_I^Q are set to 0.72 p.u., 223.5 p.u., 16.5 p.u., and 16.5 p.u., respectively, while the parameters for the simulated dataset remain unchanged. By comparing the error obtained when the ANN is trained using the transfer learning method shown in Fig. 19 to the error obtained when the ANN is trained solely on simulated data as presented in Fig. 11, it can be observed that the ANN trained using the proposed method accurately estimates the converter admittances even when the control parameters in the two datasets differ.

In this study, the control parameters are carefully selected so that the admittances show significant deviations compared to the simulation results, while still maintaining the overall frequency trend. Within this range, the transfer learning approach demonstrates high accuracy, as the pre-trained models effectively adapt through fine-tuning with data from real-time simulations. However, as the admittances derived from the LTI model deviate further, the model's accuracy may decline due to the limited representation of such extreme cases in the training dataset. To mitigate this, future work will focus on expanding the range of control parameter variations in simulations and exploring adaptive model updating strategies.

To effectively utilize the framework outlined in this study, it is recommended to initially apply a trial-and-error approach to identify a set of control parameters that produce an admittance pattern closely aligned with the simulated data. The framework will perform more accurately if the admittances generated from these initial parameters are consistent with the real system or simulated data. This approach allows for better fine-tuning and ensures that the transfer learning models operate in a representative range of operating conditions, thereby, improving the framework's overall reliability and performance. Extending this trial process can also help avoid potential parameter discrepancies between the LTI model and the real-time measurements, resulting in more robust and accurate admittance estimates.

IV. Conclusion

This paper introduces a transfer learning methodology for impedance characterization of MMCs. The outlined procedure employs LTI state-space modeling and closed-box impedance measurements to capture impedance responses. However, the accuracy of impedance estimation by the LTI model is compromised due to practical constraints, and obtaining impedance measurements through simulations can be time-consuming. Given the limited data availability of the impedance characteristics obtained through simulations, the proposed method accurately predicts the impedance characteristics at different operating points and frequency steps. Furthermore, using several smaller ANN models rather than a single ANN model over the entire frequency range appears to be beneficial in predicting the impedance responses. The proposed transfer learning framework has shown advantages over traditional ANN methods, particularly in scenarios where certain converter parameters are kept confidential by manufacturers.

References

[1] A. Sajadi, R. W. Kenyon, and B.-M. Hodge, "Synchronization in electric power networks with inherent heterogeneity up to 100% inverter-based renewable generation," *Nat. Commun.*, vol. 13, no. 1, 2022, Art. no. 2490.

[2] X. Wang and F. Blaabjerg, "Harmonic stability in power electronic-based power systems: Concept, modeling, and analysis," *IEEE Trans. Smart Grid*, vol. 10, no. 3, pp. 2858–2870, May 2019.

[3] X. Wang, L. Harnefors, and F. Blaabjerg, "Unified impedance model of grid-connected voltage-source converters," *IEEE Trans. Power Electron.*, vol. 33, no. 2, pp. 1775–1787, Feb. 2018.

[4] B. Wen, D. Dong, D. Boroyevich, R. Burgos, P. Mattavelli, and Z. Shen, "Impedance-based analysis of grid-synchronization stability for three-phase paralleled converters," *IEEE Trans. Power Electron.*, vol. 31, no. 1, pp. 26–38, Jan. 2016.

[5] Y. Liao and X. Wang, "Stationary-frame complex-valued frequency-domain modeling of three-phase power converters," *IEEE J. Emerg. Sel. Topics Power Electron.*, vol. 8, no. 2, pp. 1922–1933, Jun. 2020.

[6] J. Sun, "Impedance-based stability criterion for grid-connected inverters," *IEEE Trans. Power Electron.*, vol. 26, no. 11, pp. 3075–3078, Nov. 2011.

[7] J. Khazaei, M. Beza, and M. Bongiorno, "Impedance analysis of modular multi-level converters connected to weak AC grids," *IEEE Trans. Power Syst.*, vol. 33, no. 4, pp. 4015–4025, Jul. 2018.

[8] J. Pedra, L. Sainz, and L. Monjo, "Three-port small signal admittance-based model of VSCs for studies of multi-terminal HVDC hybrid AC/DC transmission grids," *IEEE Trans. Power Syst.*, vol. 36, no. 1, pp. 732–743, Jan. 2021.

[9] S. Shah and L. Parsa, "Impedance modeling of three-phase voltage source converters in DQ, sequence, and phasor domains," *IEEE Trans. Energy Convers.*, vol. 32, no. 3, pp. 1139–1150, Sep. 2017.

[10] Ö. C. Sakinci, A. Lekić, and J. Beerten, "Generalized impedance-based AC/DC power system modeling for harmonic stability analysis," *Int. J. Elect. Power Energy Syst.*, vol. 143, 2022, Art. no. 108456.

[11] A. Lekić and J. Beerten, "Generalized multiport representation of power systems using ABCD parameters for harmonic stability analysis," *Electric Power Syst. Res.*, vol. 189, 2020, Art. no. 106658.

[12] Y. Li et al., "Machine learning at the grid edge: Data-driven impedance models for model-free inverters," *IEEE Trans. Power Electron.*, vol. 39, no. 8, pp. 10465–10481, Aug. 2024.

[13] B. Wen, D. Boroyevich, R. Burgos, P. Mattavelli, and Z. Shen, "Influence of phase-locked loop on dq frame impedance of three-phase voltage source converters and the impact on system stability," in *Proc. CPES Power Electron. Conf.*, 2013, pp. 1–11.

[14] H. Gong, D. Yang, and X. Wang, "Impact analysis and mitigation of synchronization dynamics for DQ impedance measurement," *IEEE Trans. Power Electron.*, vol. 34, no. 9, pp. 8797–8807, Sep. 2019.

[15] H. Gong, D. Yang, and X. Wang, "Impact of synchronization phase dynamics on DQ impedance measurement," in *Proc. IEEE 19th Workshop Control Model. Power Electron.*, 2018, pp. 1–7.

[16] M. Zhang, X. Wang, D. Yang, and M. G. Christensen, "Artificial neural network based identification of multi-operating-point impedance model," *IEEE Trans. Power Electron.*, vol. 36, no. 2, pp. 1231–1235, Feb. 2021.

[17] M. Zhang, Q. Xu, and X. Wang, "Physics-informed neural network based online impedance identification of voltage source converters," *IEEE Trans. Ind. Electron.*, vol. 70, no. 4, pp. 3717–3728, Apr. 2023.

[18] Y. Li et al., "Neural network models and transfer learning for impedance modeling of grid-tied inverters," in *Proc. IEEE 13th Int. Symp. Power Electron. Distrib. Gener. Syst.*, 2022, pp. 1–6.

[19] M. Zhang, Y. Zhang, and Q. Xu, "Transfer learning based online impedance identification for modular multilevel converters," *IEEE Trans. Power Electron.*, vol. 38, no. 10, pp. 12207–12218, Oct. 2023.

[20] J. Lyu, Y. Rao, Z. Wang, J. Dai, and X. Cai, "Data-driven impedance identification and stability online assessment of wind farm connected with MMC-HVDC," *IEEE Trans. Ind. Appl.*, vol. 60, no. 2, pp. 2567–2576, Mar./Apr. 2024.

[21] T. K. Vrana, Y. Yang, D. Jovcic, S. Dennetière, J. Jardini, and H. Saad, "The CIGRE B4 DC grid test system," *Electra*, vol. 270, no. 1, pp. 10–19, 2013.

[22] G. Bergna-Diaz, J. Freytes, X. Guillaud, S. D'Arco, and J. A. Suul, "Generalized voltage-based state-space modeling of modular multilevel converters with constant equilibrium in steady state," *IEEE J. Emerg. Sel. Topics Power Electron.*, vol. 6, no. 2, pp. 707–725, Jun. 2018.

[23] G. Bergna-Diaz, D. Zonetti, S. Sanchez, R. Ortega, and E. Tedeschi, "PI passivity-based control and performance analysis of MMC multiterminal HVDC systems," *IEEE J. Emerg. Sel. Topics Power Electron.*, vol. 7, no. 4, pp. 2453–2466, Dec. 2019.

[24] J. Freytes, "Small-signal stability analysis of modular multilevel converters and application to MMC–based multi-terminal DC grids," Ph.D. dissertation, Ecole Centrale de Lille, Villeneuve-d'Ascq, France, 2017.

[25] A. Lekić, H. Ergun, and J. Beerten, "Initialisation of a hybrid AC/DC power system for harmonic stability analysis using a power flow formulation," *High Voltage*, vol. 5, no. 5, pp. 534–542, 2020.

[26] A. B. Salas, "Control interactions in power systems with multiple VSC HVDC converters," Ph.D. thesis, 2018. [Online]. Available: https://kuleuven.limo.libis.be/discovery/fulldisplay?docid=lirias1987945&context=SearchWebhook&vid=32KUL_KUL:Lirias&lang=en&search_scope=lirias_profile&adaptor=SearchWebhook&tab=LIRIAS&query=any,contains,LIRIAS1987945&offset=0

[27] Y. Wang, X. Wang, F. Blaabjerg, and Z. Chen, "Harmonic instability assessment using state-space modeling and participation analysis in inverter-fed power systems," *IEEE Trans. Ind. Electron.*, vol. 64, no. 1, pp. 806–816, Jan. 2017.

[28] Ö. C. Sakinci and J. Beerten, "Generalized dynamic phasor modeling of the MMC for small-signal stability analysis," *IEEE Trans. Power Del.*, vol. 34, no. 3, pp. 991–1000, Jun. 2019.

[29] P. K. Mogensen et al., *Julianlsolvers/nlsolve.jl*, V4.5.1, Dec. 2020. [Online]. Available: https://zenodo.org/records/4404703

[30] J. Revels, M. Lubin, and T. Papamarkou, "Forward-mode automatic differentiation in julia," 2016, *arXiv:1607.07892*.

[31] T. Maguire, B. Warkentin, Y. Chen, and J. Hasler, "Efficient techniques for real time simulation of MMC systems," in *Proc. Int. Conf. Power Syst. Transients*, 2013, pp. 1–7.

[32] K. Ou et al., "Research and application of small time-step simulation for mmc VSC-HVDC in RTDS," in *Proc. Int. Conf. Power System Technol.*, 2014, pp. 877–882.

[33] Y. Qi, H. Ding, Y. Zhang, X. Shi, and A. M. Gole, "Identification of sub-synchronous interaction in MMC systems using frequency scanning," in *Proc. IEEE Power Energy Soc. Gen. Meeting*, 2020, pp. 1–5.

[34] X. Jiang and A. Gole, "A frequency scanning method for the identification of harmonic instabilities in HVDC systems," *IEEE Trans. Power Del.*, vol. 10, no. 4, pp. 1875–1881, Oct. 1995.

[35] Y. Qi, A. Gole, H. Ding, and Y. Zhang, "Evaluation of the accuracy of real-time digital simulator voltage source converter models determined from frequency scanning," in *Proc. IPST Conf. Seoul*, 2017. [Online]. Available: https://www.ipstconf.org/Proc_IPST2017.php

[36] T. Akiba, S. Sano, T. Yanase, T. Ohta, and M. Koyama, "Optuna: A next-generation hyperparameter optimization framework," in *Proc. 25th ACM SIGKDD Int. Conf. Knowl. Discov. Data Mining*, 2019, pp. 2623–2631.

[37] Y. Liao and X. Wang, "Impedance-based stability analysis for interconnected converter systems with open-loop RHP poles," *IEEE Trans. Power Electron.*, vol. 35, no. 4, pp. 4388–4397, Apr. 2020.

[38] J. Yosinski, J. Clune, Y. Bengio, and H. Lipson, "How transferable are features in deep neural networks?," in *Proc. Adv. Neural Inf. Process. Syst.*, 2014, vol. 27, pp. 3320–3328.